Chemosphere 247 (2020) 125867

Contents lists available at ScienceDirect

Chemosphere

journal homepage: www.elsevier.com/locate/chemosphere

The removal of phosphate by thermally treated red mud from water: The effect of surface chemistry on phosphate immobilization

Jui-Yen Lin [a, b], Minsoo Kim [c], Dan Li [c], Hyunook Kim [c], Chin-pao Huang [a, *]

[a] Department of Civil and Environmental Engineering, University of Delaware, Newark, DE, 19716, United States
[b] Department of Chemical Engineering, National Cheng Kung University, Tainan, 701, Taiwan
[c] Department of Environmental Engineering, University of Seoul, Seoul, 130-743, South Korea

HIGHLIGHTS

- Dehydration, decarbonatization, and formation of new silicate/aluminate phases occurred.
- Surface acidity increased after phase transformation at high temperature.
- Thermal activation increased phosphorus adsorption density.
- Multilayer adsorption model better describe phosphorus uptake by thermally treated red mud.

GRAPHICAL ABSTRACT

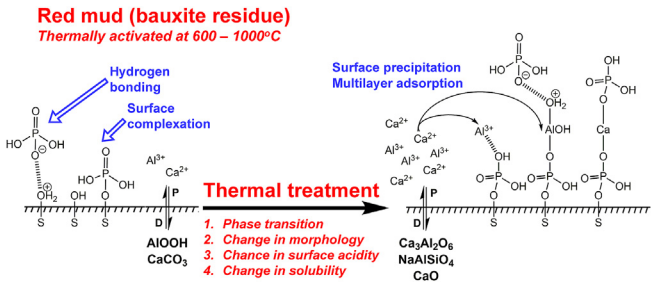

ARTICLE INFO

Article history:
Received 15 August 2019
Received in revised form
3 January 2020
Accepted 6 January 2020
Available online 8 January 2020

Handling Editor: Y Yeomin Yoon

Keywords:
Bauxite residue
Surface acidity
Electric double layer
Surface precipitation
Sorption

ABSTRACT

This study investigated thermal treatment of red mud (RM) and its effect on phase composition, surface property, and sorption capacity exemplified by phosphate. Dehydration (~600 °C), decomposition of carbonate minerals (700 °C–800 °C), and silicate/aluminate formation (900 °C–1000 °C) occurred upon thermal treatment of RM. Grain growth and vitrification that rendered initial morphology changes and decreased the specific surface area of RM from 26.5 to 4.1 m^2/g when treated from 600 to 1000 °C, respectively. Surface acidity, i.e., intrinsic acidity constant and surface acidity density, decreased as well after thermal treatment at 600 °C due to burnouts of organics then increased upon further elevated-temperature treatment because of phase transformation. Thermal activation enhanced phosphate adsorption density (μmol/m^2). Multilayer sorption aided by leached metal ions was responsible for phosphate immobilization.

1. Introduction

Red mud (RM), the residue of bauxite refinery *via* Bayer process, has become one of the largest industrial wastes in the world due to high demand of aluminum. Red mud is the insoluble fine solids generated in the caustic digestion of bauxite, where aluminum oxide is extracted under high temperature and pressure (de Souza et al., 2013). The chemical composition of RM, varying with the source of bauxite ores and parameters of refinery process, are typically iron oxide, aluminum oxide, silicon oxide, titanium oxide, and calcium oxide (Pontikes and Angelopoulos, 2013). For every ton of alumina produced, approximately 1–1.5 tons (dry weight) of RM

* Corresponding author.
E-mail address: huang@udel.edu (C.-p. Huang).

https://doi.org/10.1016/j.chemosphere.2020.125867
0045-6535/

are generated. Globally, the total amount of RM was estimated to be 3000 million tons in 2010, with an annual production of 140 million tons (International Aluminium Institute, 2015). Currently, landfill is the major way to dispose RM, which may account for 3% of alumina production cost. However, the alkaline RM could contaminate lands and streams (Winkler et al., 2018; Di Carlo et al., 2019). Considerable efforts have been made to manage RM by considering sustainability, for example, extraction of valuable elements (Liu and Naidu, 2014), use as construction materials (Tsakiridis et al., 2004), soil amendments (Feigl et al., 2017), adsorbents, and catalysts upon modification (Wang et al., 2008). In water treatment, RM adsorbents have shown great potential in removing metal ions (*e.g.*, lead, cadmium, copper, zinc, and chromium) and nonmetallic species (*e.g.*, phosphate, arsenic, boron, nitrate, and fluoride) (Bhatnagar et al., 2011).

In order to enhance the adsorption capacity and minimize its impact to the environment, red mud needs to be activated or pretreated prior to use as adsorbent. Methods for the pretreatment/activation of red mud can be categorized as acidification, neutralization, and thermal treatment (Howe et al., 2011). Acidifying RM with inorganic acid dissolves calcite and cancrinite phases, leading to an increase in specific surface area and adsorption capacity (Liang et al., 2014). Treating RM liquor with pressurized carbon dioxide easily minimizes the causticity through conversion of alkaline metal oxides to carbonates (Han et al., 2017). Seawater neutralization eliminates excess alkalinity of RM by precipitation of calcium/magnesium hydroxide and (hydroxy)carbonate (Rai et al., 2013). Meanwhile, layered double hydroxides (LDHs) could be formed to enhance the adsorption capacity toward anionic pollutants (Palmer et al., 2010).

Thermal treatment alters the physical and chemical properties of RM through phase transition. The mineralogical variation upon annealing involves dehydration of hydroxides, incineration of carbonates, formation of mixed oxide phases, and reduction of ferric minerals (Sglavo et al., 2000; Liao et al., 2016). The adsorption capacity of thermally-activated RM toward Ni(II), Cd(II), Mn(II) and Cu(II) has been reported to be superior than plain RM (Smiljanić et al., 2010; Conceição et al., 2016; Chen et al., 2016; Yang et al., 2018). Furthermore, granular RM-based adsorbents, prepared by sintering with the addition of fly ash and clay, are easier to administrate than powdered RM (Tor et al., 2009; Zhao et al., 2012). However, the above studies only evaluated the adsorptive performance of RM based on isotherms, kinetics, and regeneration. Little information is available on the correlation between the treating temperature and mineralogy and surface chemistry of RM and its effects on ion adsorption mechanism.

Consequently, this work aimed at studying the effects of annealing temperature on the physical-chemical properties of RM and the uptake of phosphate, a limiting nutrient that causes eutrophication (Elser et al., 2007). The phosphate-laden RM may behave as a slow-release fertilizer in soil amendment applications (Yao et al., 2013; Liu et al., 2019). The annealing temperature range studied was from 600 to 1000 °C as to induce prominent phase transformation. It is hypothesized that phase transition will affect phosphate adsorption capacity because of change in surface morphology, phase composition and energy. The effect of activating temperature on the mineralogy, morphology, and surface acidity of RM was studied in terms of phosphate immobilization.

2. Materials and methods

2.1. Preparation of annealed RMs

Red mud samples were provided by Cheong-Ho Environment Development Co., Ltd., South Korea. To ensure the homogeneity, RM was manually ground using an agate mortar and pestle and particles collected after passing through a 150-μm sieve (No. 100). The fine RM was neutralized batch-wise using dilute hydrochloric acid (10^{-3} M) at a solid to liquid ratio of 10 g/L several times until pH of the supernant was <8.5, and then washed with deionized water to remove additional salts and acid attached on the RM surface. Dried neutralized RM samples at 60 °C for at least 12 h (denoted as RM60). Annealing at >1000 °C would be energy intensive and further decreased the specific surface area, therefore the activation temperature studied was between 600 °C and 1000 °C, which was the typical temperature range for RM activation (Liu et al., 2011). RM60 sample (10 g) was annealed in a muffle furnace at 600, 700, 800, 900, and 1000 °C, respectively, for 1 h at a ramping rate of 5 °C/min. The thermally treated RM samples were assigned as RM600, RM700, RM800, RM900, and RM1000, respectively.

2.2. Characterization

The chemical composition of RM samples was characterized using X-ray fluorescence (XRF, Supermini 200, Rigaku Co., TX, USA) under helium atmosphere. X-ray diffractometer (XRD, Bruker D8 Discover, Bruker AXS Inc., WI, USA) was used to characterize the prominent crystal phases of all annealed RM samples. The wavelength of the X-ray was 1.54 Å, generated by CuKα radiation (40 kV, 40 mA). The specific surface area and pore volume of RM samples were determined using Micromertics ASAP 2020 (Micromertics Instrument Co., GA, USA). RM was freeze-dried for 2 days (Benchtop freeze-dryer, Millrock Technology Inc., NY, USA) to completely remove the moisture prior to N_2 adsorption measurement. The hysteresis loop of $N_{2(g)}$ adsorption and desorption was acquired at 77.54 K. Brunauer–Emmett–Teller (BET) model and Barrett-Joyner-Halenda (BJH) model were used to calculate the specific surface area and pore size distribution, respectively. Both particle size and zeta potential (ζ) of annealed RM were characterized using a Nanosizer (Zetasizer 3000, Malvern, PA, USA). For particle size measurement, RM suspension was prepared using deionized water at a solid to liquid ratio of 0.1 g/L, added a few drops of Nonidet P40 Substitute as dispersing agent, then ultrasonically agitated to minimize aggregation. For zeta potential measurement, 0.2 g of annealed RM, specific amount of 0.2 M HCl and NaOH, and 20 mL of electrolyte (1×10^{-2} M, 4×10^{-2} M and 1×10^{-1} M NaCl) were mixed in 50 mL LDPE tube. The suspension was shaken for 24 h to reach equilibrium prior to zeta potential measurement. The morphology of annealed RM was examined using a scanning electron microscope (SEM, Hitachi SU8010).

2.3. Phosphate uptake experiments

The phosphate solution, containing 10^{-2} M NaCl (NaCl, Alfa Aesar) as background ionic strength, was prepared using monosodium phosphate (NaH_2PO_4, Alfa Aesar). Forty mL of phosphate solution and 0.04 g annealed RMs were mixed together in a 50-mL LDPE tube to yield a solid to liquid ratio of 1 g/L. Specific amount of 0.5-M HCl and 0.5-M NaOH were added to the mixture to reach desired equilibrium pH values. The suspensions were mixed on a shaker under ambient condition for 24 h. Afterwards, recorded the equilibrium pH and collected the filtrate using nylon membrane filters with a pore size of 0.45 μm. The phosphate concentration in the filtrate was determined by the vanadomolybdo phosphoric acid colorimetric method. A spectrophotometer (HACH DR-2000, Cole-Parmer, IL, USA) was used to measure the absorbance of the samples at 430 nm.

3. Results and discussion

3.1. Effect of thermal treatment on composition, mineralogy, and surface area

Table S1 shows the chemical composition of RM60 in terms of metal oxides. The Korean RM has a rather low Fe_2O_3 content (9.59 wt%) compared to typical RM (40 wt%) (Pontikes and Angelopoulos, 2013; Liu et al., 2011) because of origin of bauxite ores and refining processes. Fig. 1a~f shows that the mineralogical composition of RM. RM60 comprises of several common minerals, including anatase (TiO_2, PDF#00-021-1272), boehmite (γ-AlOOH, PDF#01-074-6248), calcite ($CaCO_3$, PDF#00-055-0586), hematite (α-Fe_2O_3, PDF#00-033-0664), natrodavyne ($Na_3Al_3SiO_{12}\cdot Na_2CO_3$, PDF#00-015-0469), and quartz (SiO_2, PDF#00-046-1045). Change of crystal phases was insignificant when treating RM at below 700 °C. Increasing the temperature to >900 °C eliminated all pre-existing crystal phases but hematite, and brought about nepheline ($NaAlSiO_4$, PDF#01-083-2372), tricalcium aluminate ($Ca_3Al_2O_6$, PDF#00-032-0150), and calcium silicate ($CaSiO_3$, PDF#01-075-5002). Fig. 1g depicts the normalized diffraction intensity of minerals as a function of temperature. Results showed significant variation of mineralogical composition with temperature (Note: pre-existing phases were normalized with respect to RM60 and newly formed phases were normalized with respect to RM1000). The diffraction intensity of hematite steadily increased with increase in temperature due to thermally induced grain growth or decomposition of iron-substituted clay minerals (Nodari et al., 2007). Boehmite, present only at 60 °C, dehydrated and formed Al_2O_3 at > 500 °C (Eq. (1)) (Lamouri et al., 2017). The relative intensity of anatase remained constant at < 800 °C and declined immediately at > 800 °C, which was attributable to phase transformation from anatase to rutile (Asiah et al., 2013). The crystallization of calcite took place *ca.* 350 °C, therefore, the intensity of calcite of RM600 was greater than that of RM60 (Radha et al., 2010). At temperature >700 °C, the minerals that contain carbonates, including calcite and natrodavyne, started to decarbonate to nepheline (Eqs. (2) and (3)) (Kurdakova et al., 2014). Incongruence phase equilibrium led to the formation of mixed metal-oxides such as nepheline, tricalcium aluminate, and calcium silicate at elevated temperature (Eq. (4)–6). Thermodynamic properties of pertinent metal oxides are shown in Tables S3 and S4 (Supporting Data, S2; Fig. S5) (Li et al., 2003).

$$2\ AlOOH_{(s)} \rightarrow \gamma\text{-}Al_2O_{3(s)} + H_2O \quad (1)$$

$$CaCO_{3(s)} \rightarrow CaO_{(s)} + CO_2 \quad (2)$$

$$Na_3Al_3Si_3O_{12}\cdot Na_2CO_{3(s)} \rightarrow 3\ NaAlSiO_{4(s)} + Na_2O_{(s)} + CO_2 \quad (3)$$

$$Na_2O_{(s)} + Al_2O_{3(s)} + 2\ SiO_{2(s)} \rightarrow 2\ NaAlSiO_{4(s)} \quad (4)$$

$$3\ CaO_{(s)} + Al_2O_{3(s)} \rightarrow Ca_3Al_2O_{6(s)} \quad (5)$$

$$CaO_{(s)} + SiO_{2(s)} \rightarrow CaSiO_{3(s)} \quad (6)$$

Particle size and surface morphology changed upon thermal treatment of RMs. Fig. S1 shows the particle size distribution of RMs annealed at different temperature; Table S2 summarizes the corresponding aspects characteristics. The geometric mean size (d_{50}) of RM increased from 325 to 800 nm after thermal treatment from 60 to 1000 °C. Increase in d_{50} could be attributed to thermal-induced grain growth. The fraction of fine particles (<100 nm) was eliminated when temperature was >900 °C, which led to decrease in effective size (d_{10}). Fig. S2 shows that the size distribution of RM could be deconvoluted into 2–3 log-normal distributions. The distinct size distribution was due to different formation pathways of RMs in the caustic digestion process. Large RM particles were mineral grains in bauxite ores while the small particles were likely formed by dissolution-precipitation mechanism during the digestion process (Hind et al., 1999). Fig. 2 reveals that the surface of RM samples treated at temperature 60–800 °C, i.e., RM60 to RM800 were covered by small irregularly shaped particles and plates. The irregularly shaped feature disappeared gradually and the grain size increased as the particles were partially interconnected, when the RM was treated at >900 °C. The morphology transition was attributable to newly formed aluminate and silicate phases.

Table 1 presents the specific surface area, pore volume, and diameter of RMs. The hysteresis loops (Fig. S3) belonged to type III and H3 isotherm defined by IUPAC, suggesting that RMs were composed of non-rigid aggregates of plate-like clays (Thommes et al., 2015). Fig. S4 shows the variation of specific surface area, pore volume and diameter as a function treatment temperature. The specific surface area of RM60 was 26.5 m^2/g, which was within the range reported by Snars and Gilkes (2009). Treatment at 800 °C reduced the specific surface area to 17.3 m^2/g, (~65% that of RM60). The specific surface area decreased further to 7.8 and 4.1 m^2/g at 900 and 1000 °C, respectively, when the microstructure was lost due mostly to crystal growth of hematite and phase transformation of silicate and aluminate phases. Fig. S4b depicts the pore volume and average pore diameter of RMs as a function of annealing temperature. The maximum pore volume and diameter occurred at 600 °C and 800 °C, respectively. Three factors, namely, burnout of carbons, vitrification, and phase transformation controlled the pore characteristics. The burnout of organics (300–500 °C) and carbonate (~750 °C) would increase both pore volume and aperture. The decomposition of calcite and natrodavyne produced calcium oxide and sodium oxide, flux agents that partially melt at T > 800 °C, which eliminated the microstructure and resulted in blockage of pores. Phase transformation of minerals was eased, aided by the partial liquefication of flux, and led to shrinkage or expansion of the crystal grain (Tarvornpanich et al., 2008).

3.2. Surface acidity

Understanding the properties of RMs-solution interface is essential to studying ion adsorption in aqueous solutions. Upon hydration, RM surface develops hydroxyl groups, which undergo protonation/deprotonation as Brønsted acids and bases (Eqs. (7) and (8)) (Corapcioglu and Huang, 1987; Park and Huang, 1987; Van Cappellen et al., 1993).

$$\underline{SOH}_2^+ = \underline{SOH}^o + H^+;\ K_{a1}^{int} = \frac{\{\underline{SOH}^o\}\{H^+\}}{\{\underline{SOH}_2^+\}} \quad (7)$$

$$\underline{SOH}^o = \underline{SO}^- + H^+;\ K_{a2}^{int} = \frac{\{\underline{SO}^-\}\{H^+\}}{\{\underline{SOH}^o\}} \quad (8)$$

where $\underline{SOH}_2^+$, $\underline{SOH}$, and $\underline{SO}^-$ are the positively charged, neutral and negatively charged surface hydroxyl species, respectively. K_{a1}^{int} and K_{a2}^{int} are the intrinsic acidity constants of the $\underline{SOH}_2^+/\underline{SOH}$ and $\underline{SOH}/\underline{SO}^-$ acid/base pairs, individually. $\{H^+\}$ refers to the surface proton concentration.

The surface acidity of RMs, herein, is calculated from the zeta-potential measurements according to the Gouy-Chapman version of electric double layer theory (Weng et al., 2001) (S2 in Supporting Data). Fig. 3 shows the zeta potential of RMs between pH 4 and 11 in 10^{-2}, 4×10^{-2} and 10^{-1} M NaCl, respectively, where the lines were

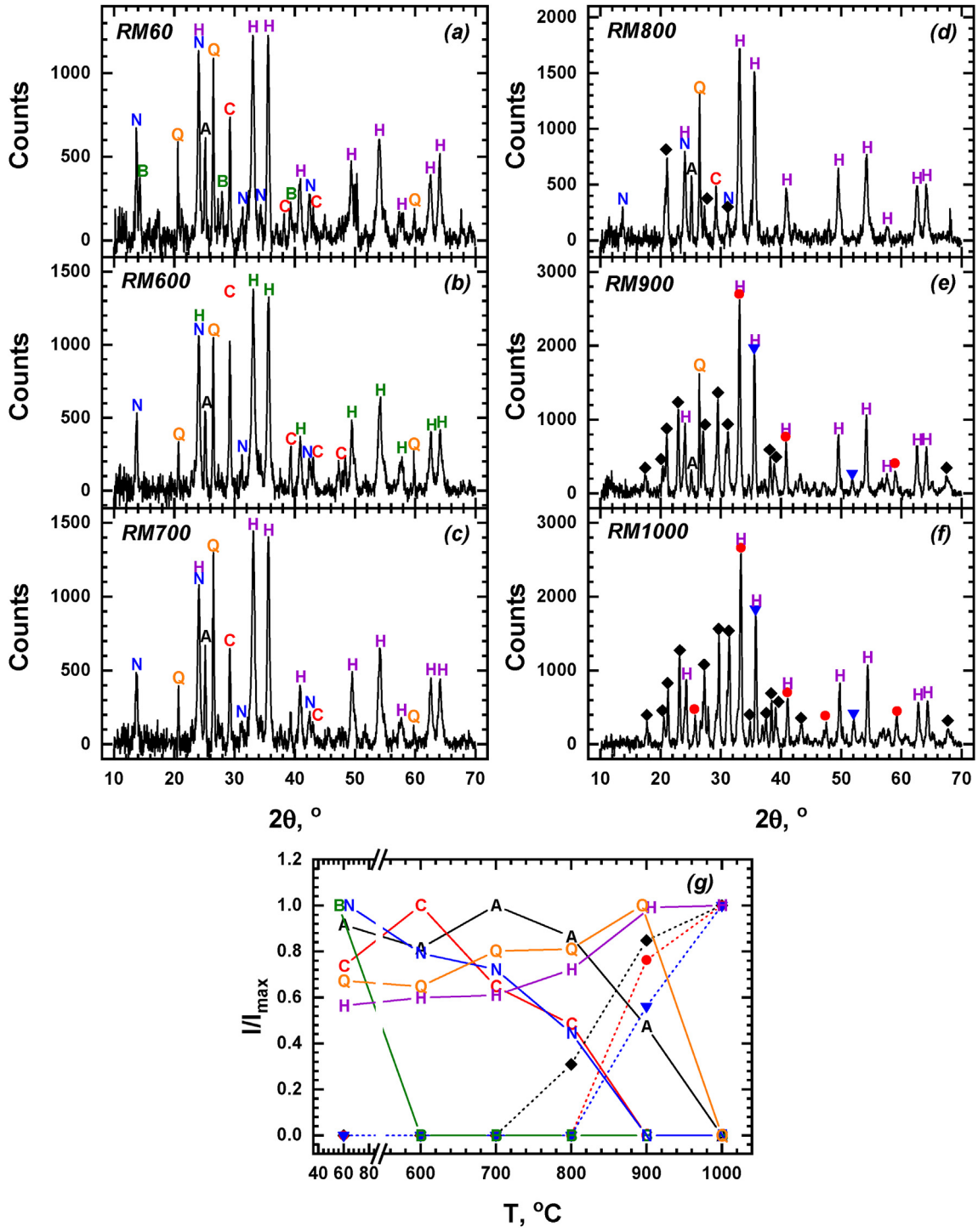

Fig. 1. XRD patterns of (a) RM60, (b) RM600, (c) RM700, (d) RM800, (e) RM900, and (f) RM1000. (g) Variation of normalized XRD intensity of major crystalline phases during thermal treatment of RM. The selected diffraction peaks (2θ) for normalization are 25.1° for anatase (TiO_2, **A**), 29.7° for bohmite (γ-AlOOH, **B**), 29.2° for calcite ($CaCO_3$, **C**), 54.2° for hematite (α-Fe_2O_3, **H**), 13.7° for natrodavyne ($Na_3Al_3Si_3O_{12}{\cdot}Na_2CO_3$, **N**), 26.5° for quartz (SiO_2, **Q**), 27.2° for nepheline ($NaAlSiO_4$, ◆), 59.1° for tricalcium aluminate ($Ca_3Al_2O_6$, ●) and 51.2° for calcium silicate ($CaSiO_3$, ▼).

fitted according to the surface acidity parameters summarized in Table 1. Overall, the surface charge of RMs could be modeled appropriately by the surface acidity model and Gouy-Chapman theory. Deviations are only apparent in RM900 and RM1000 in acid and alkaline conditions (marked with dashed lines in Fig. 3e and f), when the absolute values of ζ are smaller than the calculated. Since RM900 and RM1000 had higher surface site density than other annealed RMs (refer to $\{S_T\}$ in Table 1), specific adsorption of Na^+ and Cl^- became prominent to compensate for the charge density in the Stern layer. Even though RMs were comprised of various minerals and each of them had different pH_{pzc}, 2.0 for quartz, 4.2 for anatase, 7.8 for hematite, 8.0 for calcite, 8.5 for aluminum oxide, and 9.0 for boehmite (Kosmulski, 2018), an overall pH_{pzc} of RM was observed at the pH value where ζ was

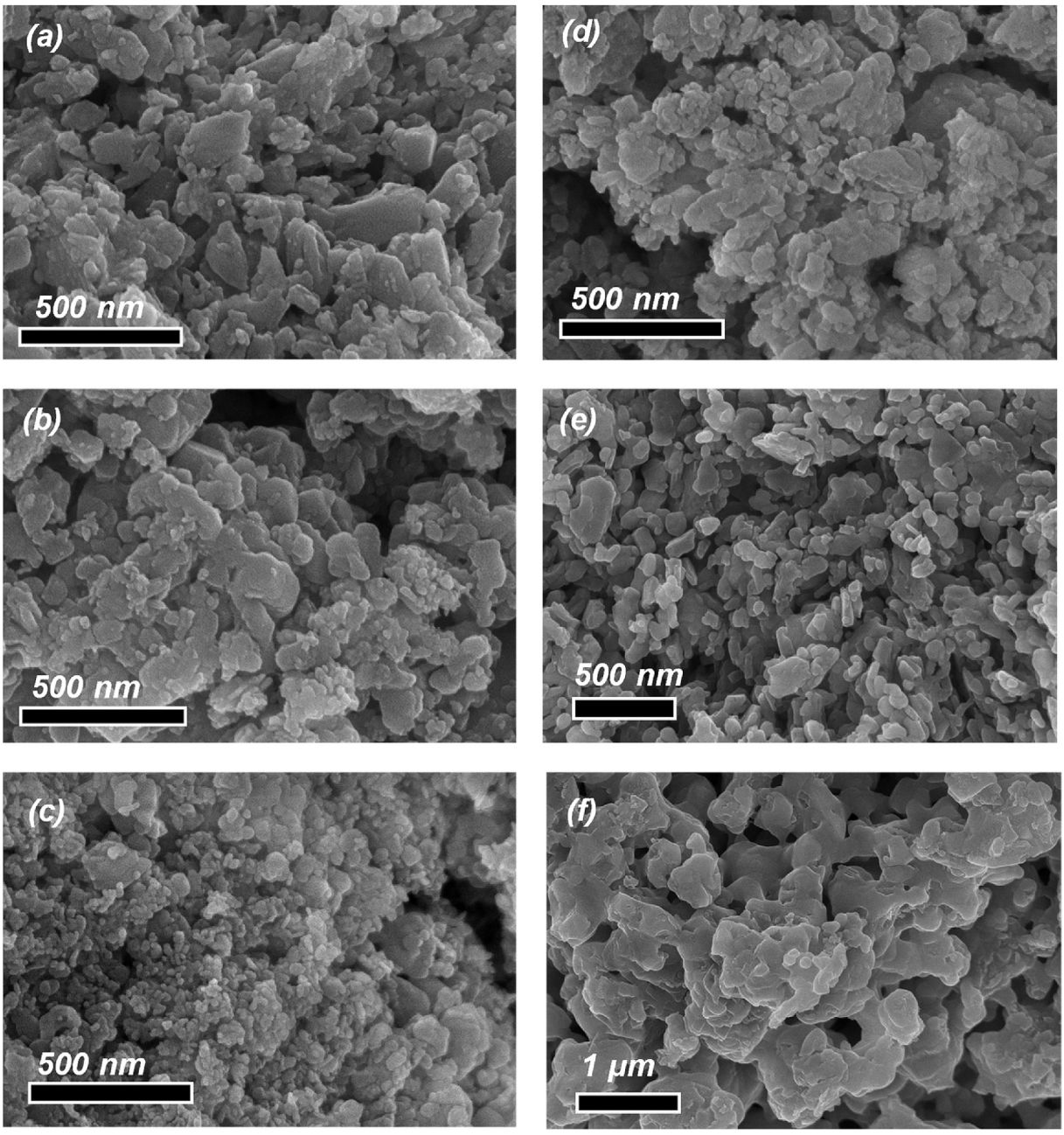

Fig. 2. Surface morphology of (a) RM60, (b) RM600, (c) RM700, (d) RM800, (e) RM900 and (f) RM1000.

Table 1
Surface characteristics of pristine and thermally-treated RM.

Specific surface area and pores						
Sample	RM60	RM600	RM700	RM800	RM900	RM1000
Surface area (m^2/g)	26.5	24.2	22.1	17.3	7.8	4.1
Pore volume (cm^3/g)	0.115	0.132	0.125	0.102	0.034	0.015
Pore diameter (nm)	13.3	15.5	16.4	17.6	16.6	14.8
Surface acidity						
Sample	RM60	RM600	RM700	RM800	RM900	RM1000
pH_{pzc}	7.43	7.71	7.67	7.56	7.46	7.10
d, Å	5.4	5.2	4.7	4.8	6.9	5.0
pK_{a1}^{int}	6.74	6.85	6.95	6.77	6.92	6.35
pK_{a2}^{int}	8.04	8.31	8.22	8.03	7.85	7.77
$\{S_T^+\}$, 10^{-7} moL/m^2	1.8	2.0	2.3	1.8	2.4	3.5
$\{S_T^-\}$, 10^{-7} moL/m^2	1.6	1.8	1.7	1.5	1.7	1.9
$\{S_T^-\}/\{S_T^-\}$	1.1	1.1	1.3	1.2	1.4	1.8

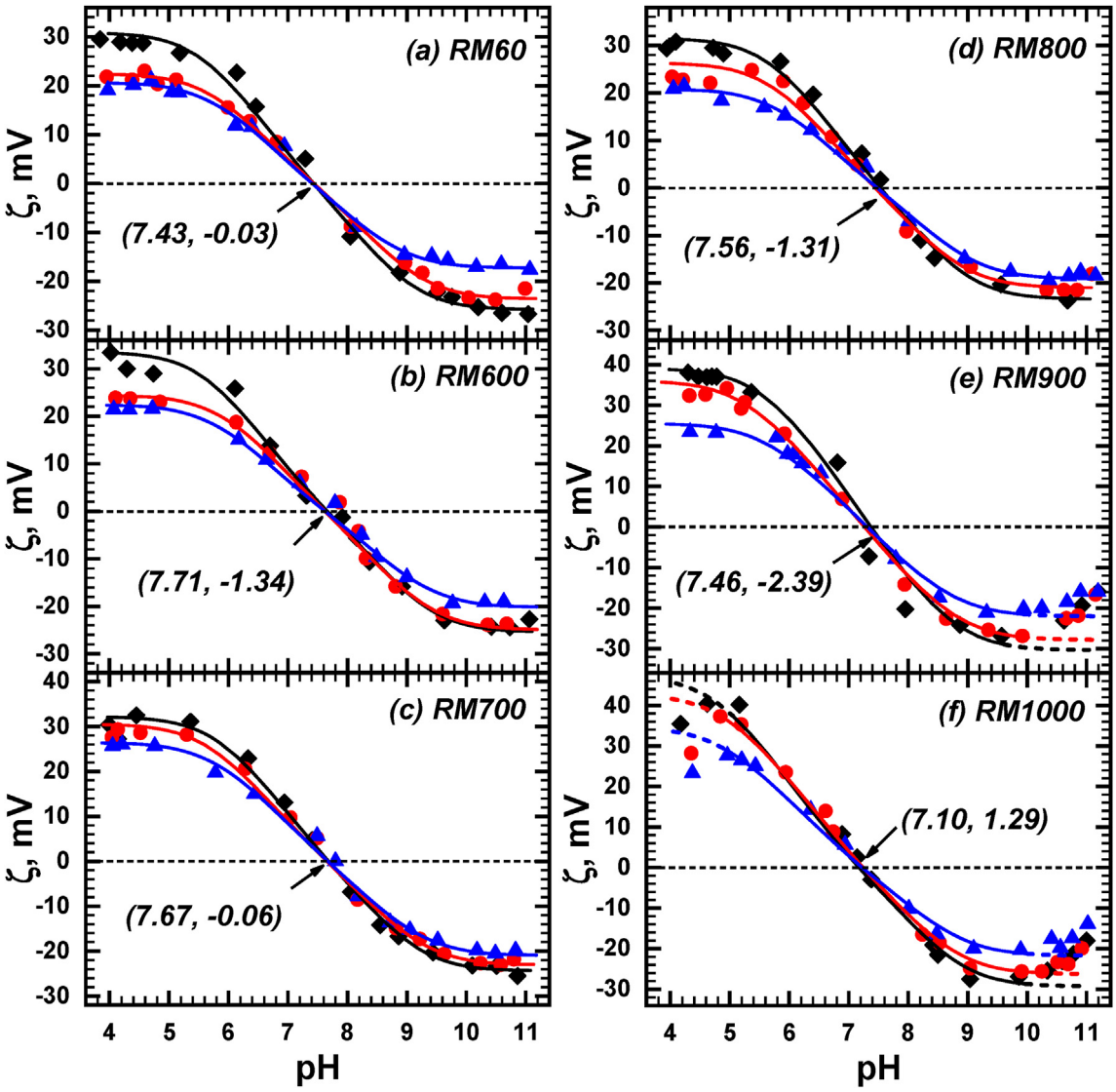

Fig. 3. Zetapotential (ζ) as a function of pH in 10^{-2} M (◆), 4 × 10^{-2} M (●), and 10^{-1} M (▲) NaCl. (X = 1 g/L, equilibrium time = 24 h, temperature = 25 °C).

independent of *I*, *i.e.*, the three curves that represent three different ionic strength intersect. At pH_{pzc}, the net surface charge equals to zero, suggesting that the surface density of positively and negatively charged groups on the RM surface, contributed from various minerals, are identical.

Fig. S7 gives the variation of pH_{pzc} and pK_a^{int} as a function of annealing temperature. The pH_{pzc} increased from 7.43 to 7.71 upon treating at 600 °C because of the burnout of acidic organic surface groups, such as formate, acetate, and oxalate (Zhong et al., 2007). In the range of 600 °C–900 °C, the pH_{pzc} decreased from 7.71 to 7.46, which was mainly caused by the decrease in pK_{a2}^{int} from 8.31 to 7.85 as pK_{a1}^{int} was fixed at 6.87 ± 0.08. Results indicated that the removal of carbonate-containing minerals allowed easy deppronation of $\underline{S}OH$ to $\underline{S}O^-$. When RM was treated at 1000 °C, the surface was mostly covered by newly formed aluminosilicate phases. Therefore, the intrinsic surface acidity constants approached those of aluminosilicate, which were 5.7 and 7.9 as pK_{a1}^{int} and pK_{a2}^{int}, respectively (Jara et al., 2005). Note that $\{\underline{S}_T^-\}$ was smaller than $\{\underline{S}_T^+\}$ for all annealed RMs, which might arise from the specific adsorption of Na^+ on $\underline{S}O^-$, or the presence of undeprotonated surface group at pH > 11.

3.3. Immobilization of phosphate

Fig. 4a~d shows the sorption density of phosphate (Γ, μmol/m^2) on annealed RMs as a function of equilibrium pH. pH is a master variable of aquatic systems (Stumm and Morgan, 1996). The pH value of common natural water is between 5 and 9, whereas that of wastewater varies widely. The surface acidity and the stability of RM significantly affect the phosphate immobilization as to be discussed later. Γ increased with annealing temperature, indicating that thermal-induced phase transformation enhanced the affinity toward phosphate. However, it should be noted that, in most cases, Γ surpassed the monolayer density of 5.78 μmoL/m^2 with respect to $H_2PO_4^-$, which hydrated ionic radius was 3.02 Å (Kiriukhin and Collins, 2002). The estimated surface coverage, in terms of $H_2PO_4^-$, increased from 10 layers on RM60 to 30 layers on RM1000 (Table S8). In other words, the mechanism of phosphate immobilization on RM surfaces was not simple monolayer adsorption in surface complexation mode. It has been reported that phosphate uptake by gibbsite (Farley et al., 1985), goethite (Ler and Stanforth, 2003; Li and Stanforth, 2000) and calcite (Liu et al., 2012; Perassi and Borgnino, 2014) is dominated by surface precipitation, when

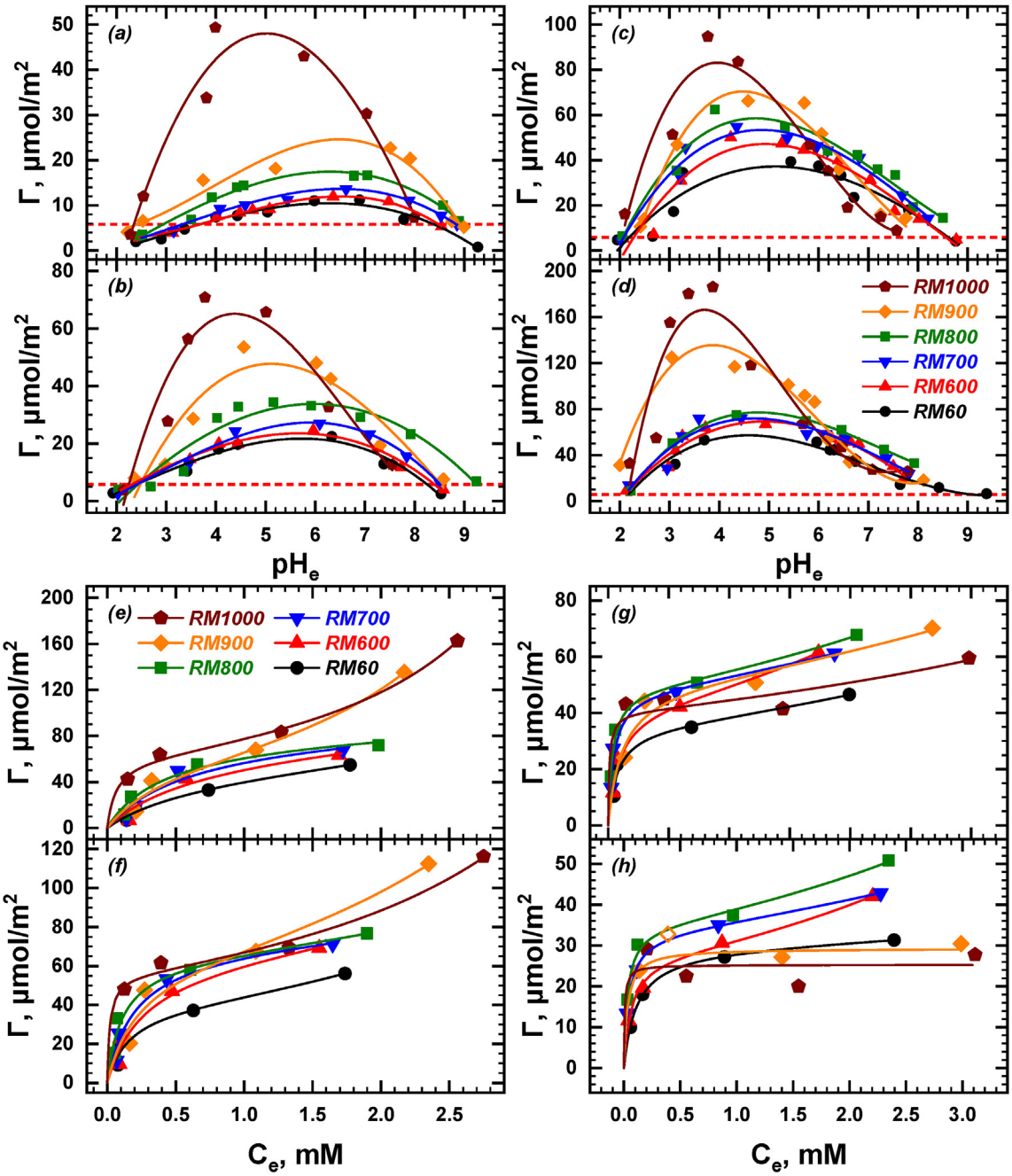

Fig. 4. Phosphate sorption density on annealed RMs as a function of equilibrium pH in the presence of initial phosphate concentration of (a) 0.32 mM, (b) 0.65 mM, (c) 1.61 mM, and (d) 3.26 mM (Dashed line represents the calculated monolayer adsorption density of $H_2PO_4^-$). Phosphate sorption isotherms of annealed RMs at (e) pH 4, (f) pH 5, (g) pH 6 and, (h) pH 7. ([NaCl] = 10 mM, X = 1 g/L, equilibrium time = 24 h, temperature = 25 °C).

both phosphate and metal ions were present in the solution at concentration higher that of the solubility limits. That is, once phosphate was fixed to the existing surface by complexation (Sø et al., 2011), subsequent adsorption of metal cations, such as metal cations, *e.g.*, Al^{3+}, Fe^{3+}, and Ca^{2+}, generated new hydrous metal oxide sites, which were available for further phosphate adsorption, and eventually led to multilayer sorption or surface precipitation. Fig. 5 shows the solubility diagram of major minerals in RM samples treated at different temperatures. Table S5 gives the solubility products (K_{sp}) used to calculate the solubility of major phases in RM. Results showed that the major phases formed during thermal treatment, i.e., $Ca_3Al_2O_6$ and $NaAlSiO_4$, were more soluble than the phases of RM60, i.e., $CaCO_3$ and AlOOH. Moreover, the solubility of phosphate minerals was lower than that of major minerals of RMs. Specifically, aluminum and calcium ions would dissolve from the minerals of RMs and precipitate with phosphate on the surface of RMs, providing an adsorption density greater than that of monolayer coverage.

The equilibrium pH affects Γ greatly as it dominates the speciation of both phosphate and RM surface. With an initial phosphate loading of 0.32 mM, when precipitation was less prominent due to lower supersaturation, the uptake of phosphate took place at pH 3 for RM1000 and pH 8 for all other RMs (Fig. 4a). Referring to the speciation of phosphate and surface group of annealed RMs in

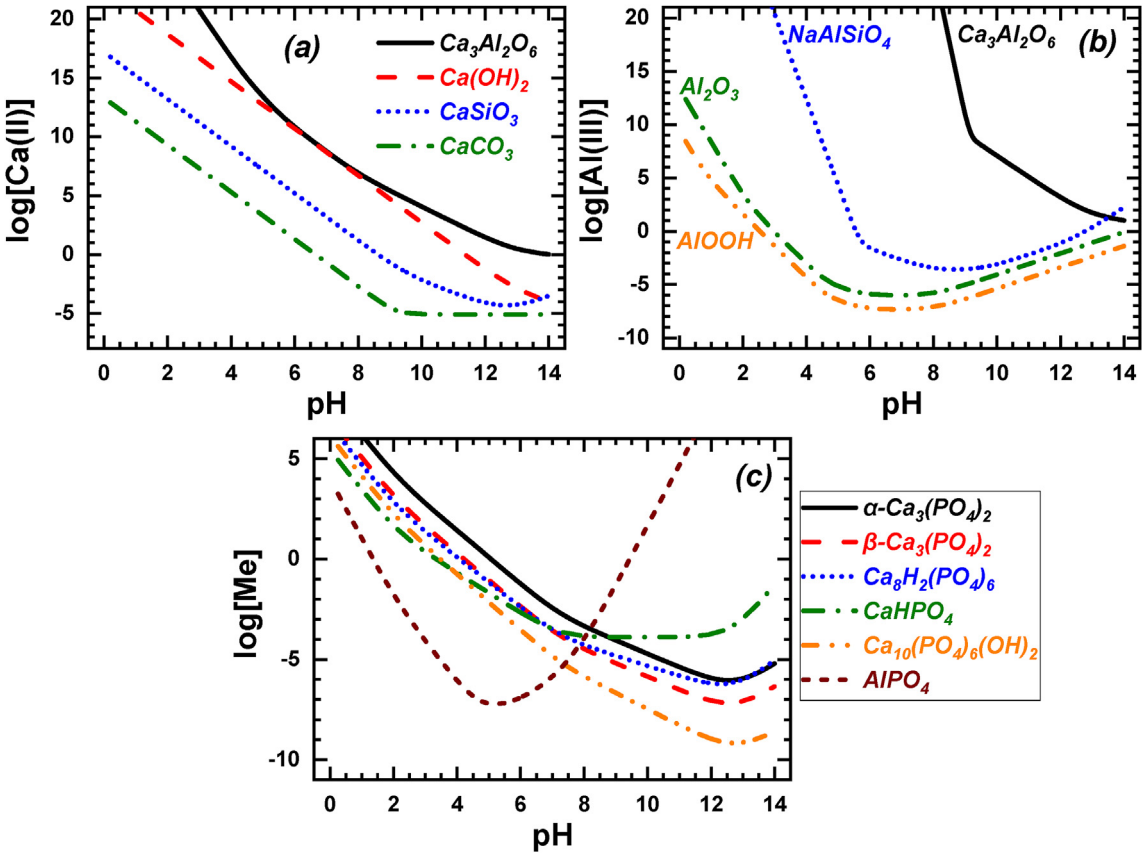

Fig. 5. Solubility diagram of (a) calcium minerals, (b) aluminum minerals, and (c) phosphate minerals of annealed RMs. Conditions: (a) [Al(II)] = 10^{-2} M, [Si(IV)] = 10^{-3} M, $P_{CO2} = 10^{-3.5}$ atm; (b) [Ca(II)] = 10^{-2} M, [Na(I)] = 10^{-2} M, [Si(IV)] = 10^{-3} M; (c) [P(V)] = 10^{-3} M.

Figs. S6 and S8, respectively, it is reasonable to assume that phosphate adsorption mainly occurred between phosphate ions ($H_2PO_4^-$, HPO_4^{2-}) and surface groups (SOH_2^+ and SOH). As the initial phosphate loading increased, surface precipitation prevailed. By plotting pH_e at maximal Γ as a function of initial phosphate loadings, $[P]_0$ (Fig. S9), it is seen that the sorption pH edge shifted downwards with respect to $[P]_0$. Table S6 shows the polynomial fitting of phosphate uptake as a function of pH ($\Gamma = a + b \times pH + c \times pH^2 + d \times pH^3$). Fig. S10 shows Γ as a function of equilibrium pH for various red mud adsorbents prepared at different temperature. The phosphate sorption characteristics onto thermally treated red mud was attributed to the following three aspects: (1) the dissolution of minerals was significant as pH decreased (Fig. 4a b); (2) the solubility of surface precipitates increased with decreasing pH (Fig. 4c); (3) the degree of supersaturation was increased with increase in initial phosphate loading.

Fig. 4e ~ h shows the phosphate sorption isotherms at various pH values. Apparently, sorption isotherms, especially for RM900 and RM1000 under acidic condition, were different from typical Langmuir and Freudlich models indicating multilayer precipitation predominance as equilibrium concentration increased. To describe phosphate sorption density as a function of equilibrium phosphate concentration (i.e., adsorption isotherm), a multilayer sorption model was adopted (Wang et al., 1998):

$$\Gamma = \frac{\Gamma_1 K_1 C_e}{(1 - K_2 C_e)[1 + (K_1 - K_2) C_e]} \quad (9)$$

where Γ is total sorption density (μmol/m^2), Γ_1 refers to adsorption density of the first homogenous layer (μmol/m^2), C_e is equilibrium phosphate concentration (mM), K_1 and K_2 are equilibrium constants for the first layer and multilayer sorption (mM^{-1}), respectively. Notably, K_1 represents the adsorption energy of the first layer. K_2 is energy involved in multilayer sorption. Note that Eq. (9) is reduced to typical Langmuir model when K_2 is negligible. Table S7 lists the fitting parameters of annealed RMs according to the multilayer sorption model. Results showed high degree of fitting experimental data by Eq. (9) with R^2 values mostly greater than 0.995, except RM900 and RM1000 at neutral pH region of 6 and 7, where the R^2 was in the range of 0.7179–0.7924. Furthermore, in the neutral pH region, both RM900 and RM1000 exhibited insignificant K_2 values, which implied that surface precipitation, namely, from the soluble Al^{3+} ions, was insignificant to co-precipitate phosphate. As shown in Fig. 5b, the solubility of major mineral phases formed on RM900 and RM1000, i.e., $NaAlSiO_4$, was at its minimum in the pH region of 6 and 7. Therefore, surface complex formation played a more important role then surface precipitation on phosphate sorption in the neutral pH region on RM900 and RM1000.

Fig. 6 sows the influence of annealing temperature on the parameters of multilayer sorption model (Eq. (9)) at pH from 4 to 7. According to Fig. 6a_1, Γ_1 was maximized at 700 °C under acidic condition and at 700–900 °C in neutral pH. Results showed that thermal treatment tuned the density of active sites and thus phosphate sorption capacity. Fig. 6b_1 clearly shows that Γ_1 decreased with pH for all annealed RMs, which was attributed in part to the speciation of both surface group and aqueous phosphate. Fig. 6b_2 suggested that the first layer equilibrium constant (K_1) of annealed RMs increased with pH and that of RM1000 was greater than all other RMs, which indicated that the prominent

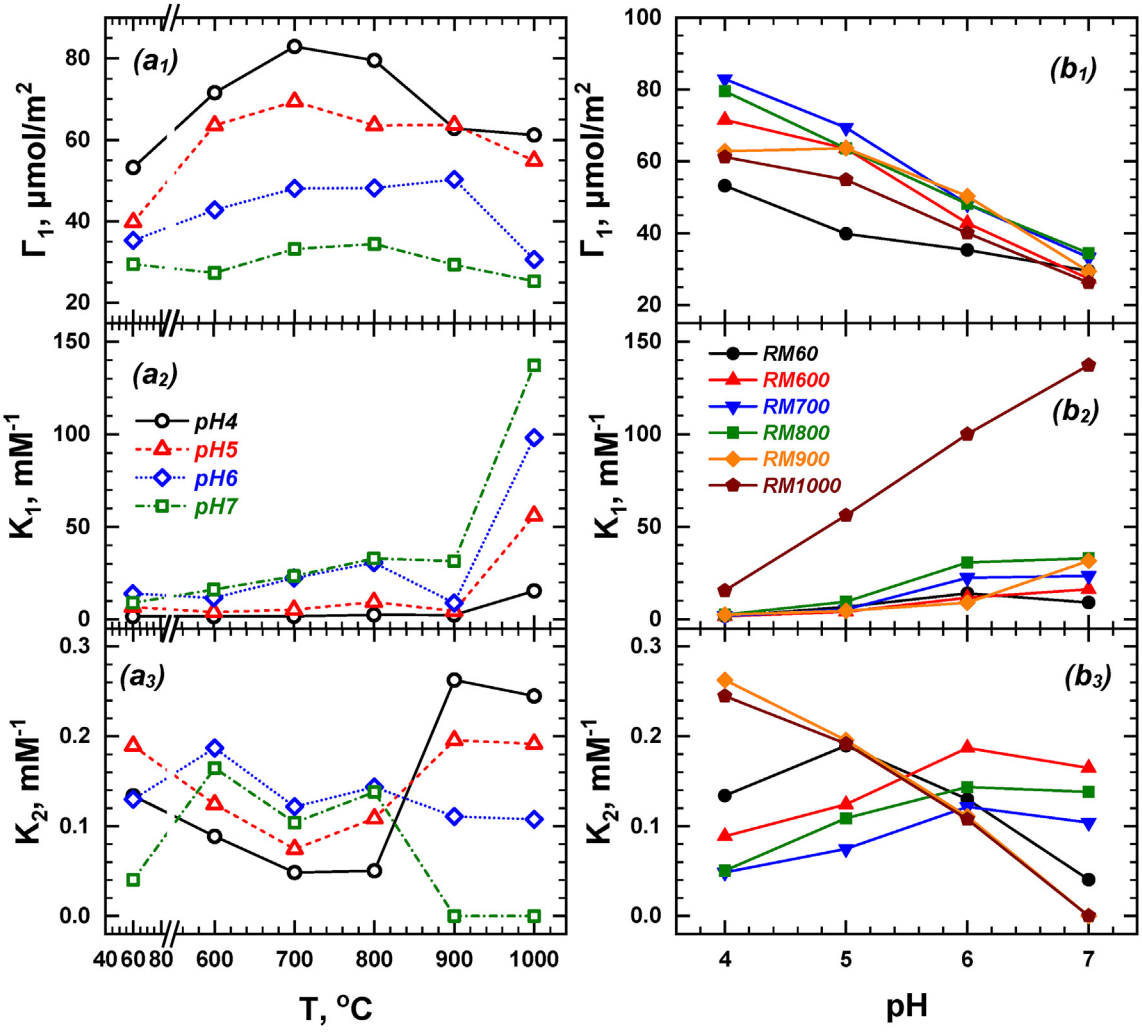

Fig. 6. Variation in parameters of multilayer sorption model as a function of (a) annealing temperature and (b) pH.

phase transformation enhanced the affinity between surface active sites and phosphate species and lowered the Gibbs free energy of adsorption ($\Delta G = -RTlnK$). Except RM1000, the K_1 values of RM60 to RM900 generally increased with annealing temperature under neutral pH but stayed rather constant under acidic condition (Fig. 6a$_2$), which reflected stronger affinity between phosphate and neutral surface group, $\underline{S}OH^0$ than that between phosphate and positive surface group, $\underline{S}OH_2^+$ (Fig. S6). Fig. 6b$_3$ shows that the K_2 of RM900 and RM1000 decreased with pH and that of RM600, RM700 and RM800 increased with pH, whereas the K_2 of untreated RM60 was in between the two groups. Results revealed that RM treated between 600 °C and 800 °C exhibited lower K_2 under acidic than neutral pH condition; in contrast, annealing RM > 900 °C K_2 decreased with pH. As indicated above, the sorption of phosphate on thermally treated red mud was complex. The build-up of multilayer sorption on RM was governed by the availability of multivalent metal ions leached from RM, the mineral dissolution rate (mineral-specific), surface species, solution pH, and total surface area (Stumm and Morgan. 1996; Mbogoro et al., 2011). However, the multilayer sorption model still could not assert the contribution of every mineral in annealed RMs explicitly. It only enabled the assessment of contribution of surface acidity/complex formation and surface co-precipitation phosphate toward phosphate removal by thermally treated red mid.

In summary, thermal treatment on RMs brought about mineral decomposition and phase transformation, which in turn altered the surface acidity and the mineral leachability of RMs. The surface acidity determined the speciation of surface groups, which played important roles in surface complexation of phosphate, *i.e.* the first homogeneous adsorption layer. Mineral leachability contributed metal ions necessary for multilayer sorption/surface precipitation.

4. Conclusion

Thermal treatment of red mud (RM) caused significant changes in chemical composition, morphology and surface property, leading to different performance in phosphate immobilization. The variation in mineralogy included dehydration (~600 °C), decomposition of carbonate minerals (700 °C–800 °C) and silicate/aluminate formation (900 °C–1000 °C). Burnout of organics and carbonates expanded pores, whereas thermally induced crystal growth and phase transformation rendered surface microstructure smooth, resulting in dramatic decrease in specific surface area. Electrophoresis as a function of pH enabled the calculation of surface site density (S_T) and intrinsic surface acidity (K_a^{int}), which were used to calculate the speciation of surface groups. The pH_{pzc} of annealed RMs was within 7.10–7.71, and the variation in surface acidity was subjected to organic burnout and phase transition. Thermal

treatment of RMs enhanced the sorption density of phosphate ($\mu mol/m^2$). Results of solubility evaluations indicated formation of new phases through annealing. Leached Al(III) and Ca(II) ions enabled bound formation with adsorbed phosphate species and created secondary adsorption sites. Therefore, multilayer sorption model described well phosphate adsorption onto annealed RMs.

CRediT authorship contribution statement

Jui-Yen Lin: Methodology, Software, Writing - original draft. **Minsoo Kim:** Resources. **Dan Li:** Resources. **Hyunook Kim:** Funding acquisition, Project administration, Writing - review & editing. **Chin-pao Huang:** Writing - review & editing, Supervision, Project administration.

Acknowledgements

The research was conducted under the support from University of Seoul, Seoul, South Korea. The authors would like to thank Ministry of Science and Technology, Taiwan for financial supports to Jui-Yen Lin under contract No. MOST-107-2917-I-006-013.

Appendix A. Supplementary data

Supplementary data to this article can be found online at https://doi.org/10.1016/j.chemosphere.2020.125867.

References

Asiah, M.N., Mamat, M.H., Khusaimi, Z., Achoi, M.F., Abdullah, S., Rusop, M., 2013. Thermal stability and phase transformation of TiO_2 nanowires at various temperatures. Microelectron. Eng. 108, 134–137.
Bhatnagar, A., Vilar, V.J.P., Botelho, C.M.S., Boaventura, R.A.R., 2011. A review of the use of red mud as adsorbent for the removal of toxic pollutants from water and wastewater. Environ. Technol. 32, 231–249.
Chen, H., Zheng, J., Zhang, Z., Long, Q., Zhang, Q., 2016. Application of annealed red mud to Mn^{2+} ion adsorption from aqueous solution. Water Sci. Technol. 73, 2761–2771.
Conceição, F., Pichinelli, B., Silva, M., Moruzzi, R., Menegário, A., Antunes, M., 2016. Cu(II) adsorption from aqueous solution using red mud activated by chemical and thermal treatment. Environ. Earth Sci. 75.
Corapcioglu, M.O., Huang, C.P., 1987. The surface acidity and characterization of some commercial activated carbons. Carbon 25, 569–578.
de Souza, K.C., Antunes, M.L.P., Couperthwaite, S.J., da Conceição, F.T., de Barros, T.R., Frost, R., 2013. Adsorption of reactive dye on seawater-neutralised bauxite refinery residue. J. Colloid Interface Sci. 396, 210–214.
Di Carlo, E., Boullemant, A., Courtney, R., 2019. A field assessment of bauxite residue rehabilitation strategies. Sci. Total Environ. 663, 915–926.
Elser, J.J., Bracken, M.E., Cleland, E.E., Gruner, D.S., Harpole, W.S., Hillebrand, H., Ngai, J.T., Seabloom, E.W., Shurin, J.B., Smith, J.E., 2007. Global analysis of nitrogen and phosphorus limitation of primary producers in freshwater, marine and terrestrial ecosystems. Ecol. Lett. 10, 1135–1142.
Farley, K.J., Dzombak, D.A., Morel, F.M.M., 1985. A surface precipitation model for the sorption of cations on metal oxides. J. Colloid Interface Sci. 106, 226–242.
Feigl, V., Ujaczki, É., Vaszita, E., Molnár, M., 2017. Influence of red mud on soil microbial communities: application and comprehensive evaluation of the Biolog EcoPlate approach as a tool in soil microbiological studies. Sci. Total Environ. 595, 903–911.
Han, Y.-S., Ji, S., Lee, P.-K., Oh, C., 2017. Bauxite residue neutralization with simultaneous mineral carbonation using atmospheric CO_2. J. Hazard Mater. 326, 87–93.
Hind, A.R., Bhargava, S.K., Grocott, S.C., 1999. The surface chemistry of Bayer process solids: a review. Colloids Surf., A 146, 359–374.
Howe, P.L., Clark, M.W., Reichelt-Brushett, A., Johnston, M., 2011. Toxicity of raw and neutralized bauxite refinery residue liquors to the freshwater cladoceran *Ceriodaphnia dubia* and the marine amphipod *Paracalliope australis*. Environ. Toxicol. Chem. 30, 2817–2824.
International Aluminium Institute, 2015. Bauxite Residue Management: Best Practice.
Jara, A.A., Goldberg, S., Mora, M.L., 2005. Studies of the surface charge of amorphous aluminosilicates using surface complexation models. J. Colloid Interface Sci. 292, 160–170.
Kiriukhin, M.Y., Collins, K.D., 2002. Dynamic hydration numbers for biologically important ions. Biophys. Chem. 99, 155–168.
Kosmulski, M., 2018. The pH dependent surface charging and points of zero charge. VII. Update. Adv. Colloid Interfac. 251, 115–138.
Kurdakova, S.V., Grishchenko, R.O., Druzhinina, A.I., Ogorodova, L.P., 2014. Thermodynamic properties of synthetic calcium-free carbonate cancrinite. Phys. Chem. Miner. 41, 75–83.
Lamouri, S., Hamidouche, M., Bouaouadja, N., Belhouchet, H., Garnier, V., Fantozzi, G., Trelkat, J.F., 2017. Control of the γ-alumina to α-alumina phase transformation for an optimized alumina densification. Bol. Soc. Esp. Ceram. V. 56, 47–54.
Ler, A., Stanforth, R., 2003. Evidence for surface precipitation of phosphate on goethite. Environ. Sci. Technol. 37, 2694–2700.
Li, H., Hrma, P., Vienna, J.D., Qian, M., Su, Y., Smith, D.E., 2003. Effects of Al_2O_3, B_2O_3, Na_2O, and SiO_2 on nepheline formation in borosilicate glasses: chemical and physical correlations. J. Non-Cryst. Solids 331, 202–216.
Li, L., Stanforth, R., 2000. Distinguishing adsorption and surface precipitation of phosphate on goethite (α-FeOOH). J. Colloid Interface Sci. 230, 12–21.
Liang, W., Couperthwaite, S.J., Kaur, G., Yan, C., Johnstone, D.W., Millar, G.J., 2014. Effect of strong acids on red mud structural and fluoride adsorption properties. J. Colloid Interface Sci. 423, 158–165.
Liu, X., Shen, F., Qi, X., 2019. Adsorption recovery of phosphate from aqueous solution by CaO-biochar composites prepared from eggshell and rice straw. Sci. Total Environ. 666, 694–702.
Liao, C.-Z., Zeng, L., Shih, K., 2016. Quantitative X-ray Diffraction (QXRD) analysis for revealing thermal transformations of red mud. Chemosphere 131, 171–177.
Liu, Y., Naidu, R., 2014. Hidden values in bauxite residue (red mud): recovery of metals. Waste Manag. 34, 2662–2673.
Liu, Y., Naidu, R., Ming, H., 2011. Red mud as an amendment for pollutants in solid and liquid phases. Geoderma 163, 1–12.
Liu, Y., Sheng, X., Dong, Y., Ma, Y., 2012. Removal of high-concentration phosphate by calcite: effect of sulfate and pH. Desalination 289, 66–71.
Mbogoro, M.M., Snowden, M.E., Edwards, M.A., Peruffo, M., Unwin, P.R., 2011. Intrinsic kinetics of gypsum and calcium sulfate anhydrite dissolution: surface selective studies under hydrodynamic control and the effect of additives. J. Phys. Chem. C 115, 10147–10154.
Nodari, L., Marcuz, E., Maritan, L., Mazzoli, C., Russo, U., 2007. Hematite nucleation and growth in the firing of carbonate-rich clay for pottery production. J. Eur. Ceram. Soc. 27, 4665–4673.
Palmer, S.J., Nothling, M., Bakon, K.H., Frost, R.L., 2010. Thermally activated seawater neutralised red mud used for the removal of arsenate, vanadate and molybdate from aqueous solutions. J. Colloid Interface Sci. 342, 147–154.
Park, S.W., Huang, C.P., 1987. The surface acidity of hydrous $CdS_{(s)}$. J. Colloid Interface Sci. 117, 431–441.
Perassi, I., Borgnino, L., 2014. Adsorption and surface precipitation of phosphate onto $CaCO_3$–montmorillonite: effect of pH, ionic strength and competition with humic acid. Geoderma 232–234, 600–608.
Pontikes, Y., Angelopoulos, G.N., 2013. Bauxite residue in cement and cementitious applications: current status and a possible way forward. Resour. Conserv. Recycl. 73, 53–63.
Radha, A.V., Forbes, T.Z., Killian, C.E., Gilbert, P.U.P.A., Navrotsky, A., 2010. Transformation and crystallization energetics of synthetic and biogenic amorphous calcium carbonate. P. Natl. Acad. Sci. USA 107, 16438–16443.
Rai, S., Wasewar, K.L., Lataye, D.H., Mukhopadhyay, J., Yoo, C.K., 2013. Feasibility of red mud neutralization with seawater using Taguchi's methodology. Int. J. Environ. Sci. Te. 10, 305–314.
Sglavo, V.M., Campostrini, R., Maurina, S., Carturan, G., Monagheddu, M., Budroni, G., Cocco, G., 2000. Bauxite 'red mud' in the ceramic industry. Part 1: thermal behaviour. J. Eur. Ceram. Soc. 20, 235–244.
Smiljanić, S., Smičiklas, I., Perić-Grujić, A., Lončar, B., Mitrić, M., 2010. Rinsed and thermally treated red mud sorbents for aqueous Ni^{2+} ions. Chem. Eng. J. 162, 75–83.
Snars, K., Gilkes, R.J., 2009. Evaluation of bauxite residues (red muds) of different origins for environmental applications. Appl. Clay Sci. 46, 13–20.
Sø, H.U., Postma, D., Jakobsen, R., Larsen, F., 2011. Sorption of phosphate onto calcite; results from batch experiments and surface complexation modeling. Geochem. Cosmochim. Acta 75, 2911–2923.
Stumm, W., Morgan, J.J., 1996. Aquatic Chemistry: Chemical Equilibria and Rates in Natural Waters, third ed. John Wiley & Sons, New York.
Tarvornpanich, T., Souza, G.P., Lee, W.E., 2008. Microstructural evolution in clay-based ceramics II: ternary and quaternary mixtures of clay, flux, and quartz filler. J. Am. Ceram. Soc. 91, 2272–2280.
Thommes, M., Kaneko, K., Neimark, A.V., Olivier, J.P., Rodriguez-Reinoso, F., Rouquerol, J., Sing, K.S.W., 2015. Physisorption of gases, with special reference to the evaluation of surface area and pore size distribution (IUPAC Technical Report). Pure Appl. Chem. 87, 1051–1069.
Tor, A., Danaoglu, N., Arslan, G., Cengeloglu, Y., 2009. Removal of fluoride from water by using granular red mud: batch and column studies. J. Hazard Mater. 164, 271–278.
Tsakiridis, P.E., Agatzini-Leonardou, S., Oustadakis, P., 2004. Red mud addition in the raw meal for the production of Portland cement clinker. J. Hazard Mater. 116, 103–110.
Van Cappellen, P., Charlet, L., Stumm, W., Wersin, P., 1993. A surface complexation model of the carbonate mineral-aqueous solution interface. Geochem. Cosmochim. Acta 57, 3505–3518.
Wang, J., Huang, C.P., Allen, H.E., Cha, D.K., Kim, D.-W., 1998. Adsorption characteristics of dye onto sludge particulates. J. Colloid Interface Sci. 208, 518–528.
Wang, S., Ang, H.M., Tadé, M.O., 2008. Novel applications of red mud as coagulant, adsorbent and catalyst for environmentally benign processes. Chemosphere 72,

1621–1635.
Weng, C.-H., Huang, C.P., Allen, H.E., Sanders, P.F., 2001. Cr (VI) adsorption onto hydrous concrete particles from groundwater. J. Environ. Eng. 127, 1124–1131.
Winkler, D., Bidló, A., Bolodár-Varga, B., Erdő, Á., Horváth, A., 2018. Long-term ecological effects of the red mud disaster in Hungary: regeneration of red mud flooded areas in a contaminated industrial region. Sci. Total Environ. 644, 1292–1303.
Yang, T., Sheng, L., Wang, Y., Wyckoff, K.N., He, C., He, Q., 2018. Characteristics of cadmium sorption by heat-activated red mud in aqueous solution. Sci. Rep.-UK 8, 13558.
Yao, Y., Gao, B., Chen, J., Yang, L., 2013. Engineered biochar reclaiming phosphate from aqueous solutions: mechanisms and potential application as a slow-release fertilizer. Environ. Sci. Technol. 47, 8700–8708.
Zhao, Y., Yue, Q., Li, Q., Xu, X., Yang, Z., Wang, X., Gao, B., Yu, H., 2012. Characterization of red mud granular adsorbent (RMGA) and its performance on phosphate removal from aqueous solution. Chem. Eng. J. 193–194, 161–168.
Zhong, F., Chen, X., Zhang, S., Li, Y., 2007. Organic acids and inorganic anions in Bayer liquors by ion chromatography after solid-phase extraction. J. Cent. South Univ. Technol. 14, 191–195.